https://doi.org/10.1016/j.resconrec.2022.106231

This is the Pre-Published Version.

Upcycling of Air Pollution Control Residue waste into cementitious product through geopolymerization technology

Muhammad Riaz Ahmad, Jiancong Lao, Jian-Guo Dai*, Dongxing Xuan, Chi Sun Poon

Department of Civil and Environmental Engineering, The Hong Kong Polytechnic University, Hung Hom, Kowloon, Hong Kong

Highlights

- APCr was recycled through geopolymerization technology
- Leaching characteristics of solidified samples were evaluated
- Geopolymerization technology successfully solidified APCr up to 80% by total solid mass
- APCr solidified samples could reach the strength in range of 18 to 48 MPa.

© 2022. This manuscript version is made available under the CC-BY-NC-ND 4.0 license http://creativecommons.org/licenses/by-nc-nd/4.0/

Upcycling of Air Pollution Control Residue waste into cementitious product through geopolymerization technology

Abstract

This study explores the possibility of using geopolymerization technology (GT) to immobilize the potentially toxic elements (PTEs e.g., Zn, Cu, Cr, As) in the APCr and convert it into useful cementitious product. To maximize its recycling, the amount of APCr in the designed product was increased gradually from 20% to 80% by the total solid mass. Leaching test showed that GT can effectively immobilize the PTEs in the APCr solidified samples without any health and environmental concerns. The compressive strength of samples can exceed 18 MPa at 28 days at a highest amount of 80% APCr through GT. Thermogravimetric analysis (TGA) results showed that solidified samples underwent mass loss due to evaporation of free and physically bound water at low temperatures (<200°C) and melting and evaporation of soluble salts in APCr at high temperatures (>800°C). Characterization of solidified samples conducted through the X-ray diffraction (XRD), Fourier transform infrared (FTIR) and Scanning electron microscopy-Energy dispersive analysis (SEM) revealed the formation of C-A-S-H and N-A-S-H gels in solidified bodies and verified that APCr was successfully solidified and embedded into the geopolymer network structure.

Keywords

Air pollution control residue; Geopolymer; solidification; Leaching; sewage sludge

1 Introduction

Incineration is a widely used and successful technique for the treatment of dewatered sewage sludge and municipal solid wastes (MSW) as it can effectively reduce volumes of wastes and generate energy. This process can eliminate the organic matter while reducing the volume of waste

by 85-90% and mass of waste by 60-90% (Leckner, 2015), which greatly helps to reduce the demand of land required for the disposal of MSW and sewage sludge waste and its related carbon footprint, especially in the heavily populated areas like Hong Kong (Woon and Lo, 2013; Xi et al., 2021; Zhuang et al., 2020). As per Hong Kong Environmental Bureau (EBHK, 2013), Hong Kong is expected to reach the designed capacities of present landfills in the near future due to the high disposal rate of wastes, and extension of these landfills will become inevitable. Hong Kong has one of the world's largest incinerator facilities to treat the dewatered sewage sludge that can incinerate nearly 2000 tonnes/day of sewage sludge. However, incineration ashes produced from these so-called waste-to-energy (W-t-E) incinerators contains several potentially toxic elements (PTEs) (Chen et al., 2021; Tang et al., 2020; Lei Wang et al., 2020). Hence, disposal of such kind of ashes into landfill without prior treatment should be evaluated.

Air pollution control residue (APCr) is regarded as a kind of industrial waste produced from these incinerators and is normally transported to waste landfill sites. It is produced during the cleaning process of flue gas in the incinerators and contains solids and fly ash which are captured downstream of acid gas treatment. It is highly alkaline and corrosive and consists of soluble anions and pollutants in a large concentration. This combination further poses problems in the treatment, recovery, and disposal of APCr (Gomes et al., 2016) and hence it is classified as a hazardous waste in several jurisdictions (Bogush et al., 2015; Chandler et al., 1997). It is estimated that the production of APCr will continue to rise due to the increase in numbers of incinerators and W-t-E plants. Thus, it has become necessary to find out the recovery and recycling options of APCr. Treatment of hazardous waste materials through solidification/stabilization (S/S) into valuable construction products is a viable and cost-effective approach (Sun et al., 2022).

S/S of industrial hazardous wastes is often conducted by using cementitious materials mainly ordinary Portland cement (Alderete et al., 2021; Clavier et al., 2021; Geng et al., 2020; Kumar and Garg, 2022; Loginova et al., 2021; Ma et al., 2020; Qian et al., 2022). Recently, GT has received increasing attention as a substitute of solidification through ordinary Portland cement (OPC) due to its potential benefits as compared to OPC e.g. (1) release of a large amount of carbon gas due to the production of Portland cement and (2) carbonation (Lange et al., 1995; Wang et al., 2019; Y.-S. Wang et al., 2020). Several studies have reported the use of geopolymer based binder for the S/S of radioactive contaminated sewage sludge ash (Kozai et al., 2021) and borate waste (Kim et al., 2021), heavy metals (Zn, Pb, and Cr) (Kozai et al., 2021; Pu et al., 2021; Xuan and Poon, 2018), municipal solid waste incineration (MSWI) fly ash (Cyr et al., 2012; Kozai et al., 2021; Liu et al., 2021; Wang et al., 2015), bottom ash (Boca Santa et al., 2016), bauxite residue and coal ash (Nguyen et al., 2022) and lead glass and lead slag (Long et al., 2021a; Nath et al., 2022; Pan et al., 2019; Sun et al., 2020; Van De Sande et al., 2020). Moreover, a comparison of sewage sludge ash and MSWI fly ash S/S through the use of geopolymer and Portland cement showed that GT was far superior in immobilization of heavy metals and the produced geopolymer based solidified products showed higher uniaxial compressive strength than its Portland cement counterpart (Fan et al., 2021; Kozai et al., 2021).

There are numerous studies available on the S/S of different types of hazardous wastes, however, very limited research is available on the recycling of APCr and its utilization as construction material in civil engineering (Bogush et al., 2020; Quina et al., 2014; Stegemann, 2014). Kourti et al., used glass-forming additives and DC plasma technology to treat the APCr and produce precursors for the geopolymers (I. et al., 2011; Kourti et al., 2010). A low-strength cement (<10 MPa) was produced by solidification of APCr through alkali-activation by mixing it with the co-

fired fuel ash (Shirley and Black, 2011). Geopolymerization technology was also helpful in immobilizing the several heavy metals (Ba, Pb, and Ni) present in the APCr (Mustard et al., 2016). Recycling of waste materials through S/S does not only reduces the burden on landfills but also eliminates the potential environmental risks associated with the disposal of hazardous wastes occurring due to leaching of the PTEs. Meanwhile, recycled waste materials through S/S can also partially reduce the demand for conventional construction materials leading to the path of sustainability and low carbon footprint (Ahmad et al., 2020c, 2020b, 2020a; Chang et al., 2022; Zentar et al., 2021; Zhang et al., 2022, 2020). In this regard, this study explores the possible use of APCr for the production of a cementitious product by immobilization of heavy metals through the geopolymerization technology (GT) (Li et al., 2017).

Therefore, this study aims to evaluate the feasibility of using GT for the upcycling of APCr waste. In recent years, a significant amount of research has been conducted on the reuse of MSWI fly ash, bottom ash, and sewage sludge ash in the cementitious system, however, very few researchers have tried to utilize the APCr through the use of GT. Hence, this study is focused to use the GT for the sustainable utilization of APCr. First, the produced APCr geopolymer pastes through S/S depict low to medium strength and can be used for the application as construction materials. Second, S/S of APCr will help to curb the landfill disposal issues and its potential environmental risks associated with the leaching of heavy metals. Furthermore, it will directly reduce the demand for virgin construction materials used in the cement and concrete application.

2 Materials and Methods

2.1 *Raw materials*

Raw materials used to prepare the solidified APCr based geopolymer paste included fly ash (FA), ground granulated blast-furnace slag (GGBS), APCr, and anhydrous sodium metasilicate (SS;

115 Na_2SiO_3-Anhydrous). Particle size distribution of raw materials determined by the Laser
116 diffraction technique is plotted in Fig. S1 (supplementary information). The mean diameter of FA,
117 GGBS, and APCr was 17.9, 12.4, and 8.5 μm with the specific surface area of 1392, 1488, and
118 6651 m^2/kg, respectively. The chemical compositions of raw materials are provided in Table 1.
119 The FA mainly consisted of SiO_2, Al_2O_3, and Fe_2O_3 (84.8%) and is classified as Class F FA as per
120 ASTM C618-19. Major compounds in GGBS are CaO (42.4%), SiO_2 (32.6%), and Al_2O_3 (14.7%),
121 whereas Na_2O (38.3%) and SO_3 (31.9%) are the main compounds in APCr.

122

123

124 Table 1. Oxide composition of FA, GGBFS and APCr (%)

Oxides	Fly ash	GGBS	APCr
SiO_2	49.7	32.6	6.19
Al_2O_3	25.1	14.7	3.57
Fe_2O_3	9.58	0.35	4.65
CaO	7.84	42.4	3.27
MgO	2.8	6.53	1.71
Na_2O	-	-	38.3
K_2O	1.53	0.41	0.57
TiO_2	1.15	0.61	0.19
P_2O_5	0.84	0.18	3.02
SO_3	0.96	1.82	31.9
Others	0.5	0.4	6.64

125

126 X-ray diffraction (XRD) patterns of FA, GGBS, and APCr are plotted in Fig. S2. APCr was
127 obtained from the T-park incinerator in Hong Kong. It was dried in an oven and then ground to
128 powder in a ball mill for four hours before solidification. The main phases in FA are crystalline
129 mullite ($3Al_2O_3 \cdot 2SiO_2$) and quartz (SiO_2) and APCr consists of thenardite (Na_2SO_4), halite (NaCl),
130 monosodium phosphate (NaH_2PO_4), and trisodium phosphate (Na_3PO_4). GGBS showed highly
131 amorphous behavior through the broad hump around 25-35º 2θ. SS of industrial-grade containing
132 2.73% of impurities, 46.52% of SiO_2, and 50.75% of Na_2O was used as an alkaline activator in this

study. The modulus ratio ($M_r = SiO_2/Na_2O$) of SS was 0.92. The loose bulk density of SS was 1.31 g/cm^3 and size of particles was between 0.25-1.0 mm. Morphology and distribution of raw materials observed by SEM are shown in Fig. S3. FA consists of sphere shape particles with smooth surface. GGBS has angular/irregular-shaped particles while the shape of APCr particles consists of partially rounded corners and a fluffy appearance.

2.2 *Mix proportions and solidification*

In this study, different dosages of APCr ranging from 20% to 80% were solidified by the GT. Total five mix proportions were prepared as shown in Table 2. One reference geopolymer mixture (G100-APCr0) without APCr was also prepared to compare the mechanical and microstructure properties with the APCr based solidified mixtures. The percentage of fly ash to slag in the reference mixture was 80:20. The amounts of GGBS and SS were kept constant for all mixtures to achieve the higher solidification efficiency whereas FA was gradually replaced APCr. The mixtures notation followed the weight percentage of geopolymer and APCr, respectively, e.g., G20-APCr80 means mixture containing 20% of geopolymer and 80% of APCr by total weight. Geopolymer consists of GGBS, FA, and SS. Here, FA, GGBS and SS act as the binder materials for the APCr. The percentage of alkali content (Na_2O) for chemical activation was kept 5.1% by the total weight of solids for all mixtures.

Table 2. Mix proportions of APCr solidified bodies

Mix ID	G:APCr (solids)	water/solids	Na_2O (% of solids)
G100-APCr0	100:0	0.33	5.1
G80-APCr20	80:20	0.33	5.1
G60-APCr40	60:40	0.33	5.1
G40-APCr60	40:60	0.33	5.1
G20-APCr80	20:80	0.33	5.1

153 The mixing process was started by dry mixing the raw materials (FA, GGBS, APCR and NS) in
154 the Hobart mixer at a low speed. After dry mixing for 3 minutes, water was gradually introduced
155 into the mixer, and mixing was carried out at a medium speed for another 3 minutes. Finally,
156 mixing was continued at a high speed for 3 minutes until a homogenous and uniform mixture was
157 obtained. Fresh mixtures were poured into plastic molds of dimensions 50×50×50 mm^3 and
158 covered with the plastics sheets to avoid the loss of moisture. All the samples were demolded after
159 24 hours of casting and stored in plastic sheets at ambient air conditions until testing.

160 *2.3 Experimental programme*

161 *Immobilization efficiency of GT (TCLP method)*

162 Immobilization efficiency of GT was characterized through the TCLP method 1311 (Toxicity
163 Characteristic Leaching Procedure for heavy metals) as per United States EPA protocol (EPA,
164 1992; Liuwei Wang et al., 2020). Before TCLP, raw APCr was digested through the aqua-regia
165 digestion medium and total heavy metal concentration was determined with the Inductively
166 Coupled Plasma-Optical Emission Spectrometer (ICP-OES, SpectroBlue). After it was found that
167 the concentration of heavy metals in APCr is higher than critical limits, solidified samples were
168 further testedfor the TCLP test. Solidified samples were crushed to small sizes and were passed
169 through a 4 mm sieve. Extraction was performed by rotating the samples capped in polypropylene
170 bottles for 18 ± 2 h at 30 ± 2 rpm in a TCLP rotator. The extraction liquid was glacial acetic acid
171 and liquid to solid ratio was 20:1. Liquid was separated by filtering the extracted liquid through
172 the 0.45 μm glass fiber filter. Liquid samples were further diluted by concentrated HNO_3 (sample
173 5:2 HNO_3) and digested. After the digestion, samples were diluted with 5% HNO_3 and filtered
174 again. The concentration of heavy metals was determined using the ICP-OES instrument. After
175 extraction, pH of leachates was also measured through the pH meter.

Mechanical testing

Samples were removed from the plastic sheets for the determination of compressive strength and tested using a compression machine (MATEST, 3000 kN) at 3 days and 28 days as per ASTM C109. All the samples were tested in triplicate at the loading rate of 1 MPa/s (Xu et al., 2021). Water absorption of samples was measured by immersing the samples into the water for 24 hours (to calculate saturated weight) and then drying in an oven at 105±2°C for 24 hours (to calculate dry weight).

Phase and microstructure characterization

Solidified samples were ground to fine powder after drying in the freeze-dryer and XRD analysis was performed using Rigaku SmartLab-Advance instrument at 200 mA and 45kV using Cu-Kα radiations. Scanning rate for all powder samples was kept at 0.02° per step using Bragg-Brentano focusing mode. Scanning of samples was carried out for the 2θ value from 5° to 75°. Samples for the XRD analysis were prepared after 28 days of ambient curing. To characterize the microstructure of solidified samples by scanning electron microscope (SEM), 28 days ambient cured samples were broken into small pieces and embedded into epoxy for polishing purposes. After polishing of samples using AutoMet 300 Grinder, samples were freeze-dried. The microstructure of samples was observed through the SEM machine (Tescan Vega 3 XMU) equipped with an EDS facility. For characterization of hydration products and unreacted phases, elemental and mapping analysis of samples was performed. The SEM analysis was performed in high vacuum conditions at a voltage value of 20 kV and a working distance of 18 mm. Thermogravimetric analysis (TGA) on the dried powder samples was performed using the Rigaku Thermo Plus EVO2 instrument. The mass of each sample was controlled around 8 mg and placed in an alumina crucible. The heating rate of samples was maintained at 10 $^{\circ}$C/min while samples

were heated from 30° to 1000 °C in argon gas conditions. Fourier-transform infrared (FTIR) analysis was conducted on the powder samples using the PerkinElmer UATR-two to identify the functional groups. The analysis was performed in the range of 400 cm^{-1} to 4000 cm^{-1} at 2 cm^{-1} resolutions.

3 Results and Discussions

3.1 Immobilization efficiency of APCr through GT

The results of total concentrations for different metals are provided in Fig. S4. Heavy metals present in APCr were Ni, Pb, Zn, As, Cd, Cr, Ba, Ag, and Cu. Some of the heavy metals e.g. Hg and Se were not detected and hence were of no concern. Among all heavy metals, the highest concentration was shown by Zn was around 1019 mg/L. The concentrations of Cu, Ba, Cr, and As were 266, 173, 99.4, and 75.5 mg/L respectively. Moreover, Pb, Ni, Ag, and Cd were also present in little amounts. Hence, it is highly suggested that APCr must undergo treatment when it is aimed to be reused for construction purposes due to the presence of high metal contents. As health and environmental risks are more associated with the presence of soluble heavy metals rather than the total concentration of heavy metals, leaching test was carried out by TCLP method to study the leaching characteristics of APCr samples solidified through GT.

The TCLP method simulates the leaching of PTEs from the landfill and is often used to measure the efficiency of solidification approaches to immobilize heavy metals. The results of TCLP method for APCr solidified bodies through GT are shown in Fig. 1a. The concentration of heavy metals leached from the APCr samples was greatly reduced when solidified through the GT. Importantly, concentrations for all leached metals were far below the regulatory limits advised by the U.S. EPA (US EPA, 2004) and Chinese standard (CN-GB, 2007) as shown in Table 3. This indicates that geopolymer is very efficient to immobilize heavy metals even at a higher percentage

of APCr of 80%. Geopolymer consists of 3D structure of aluminosilicate network of AlO_4 and SiO_4 tetrahedral units which can effectively seal the contaminants. Moreover, it has been reported that fly ash based geopolymer skeleton is normally stable under the strong acid-base environment. Besides the physical encapsulation, double-layered hydrate phases in geopolymer (e.g. calcium alumino/ferric) can interact with these metals chemically and replace them with interlayer hydroxyl (Long et al., 2021b; Luna Galiano et al., 2011).

Table 3. TCLP concentration of heavy metals and regulatory limits

Metal	TCLP concentration of heavy metals (mg/L)				Upper Limitation (mg/L)	
	G80-APCr20	G60-APCr40	G40-APCr60	G20-APCr80	U.S. EPA	CN-GB
Ag	1.54	1.58	1.65	1.69	5.0	-
As	0.80	0.84	0.85	0.85	5.0	5.0
Ba	0.04	0.04	0.06	0.17	100	100
Cd	0.03	0.04	0.04	0.04	1.0	-
Co	0.12	0.12	0.11	0.11	-	-
Cr	0.08	0.09	0.09	0.08	5.0	5.0
Cu	0.38	0.36	0.31	0.34	-	100
Mn	0.54	0.29	0.07	0.04	-	-
Ni	0.18	0.16	0.13	0.13	-	-
Pb	0.29	0.28	0.27	0.29	5.0	5.0
Zn	0.46	0.29	0.36	0.38	-	100

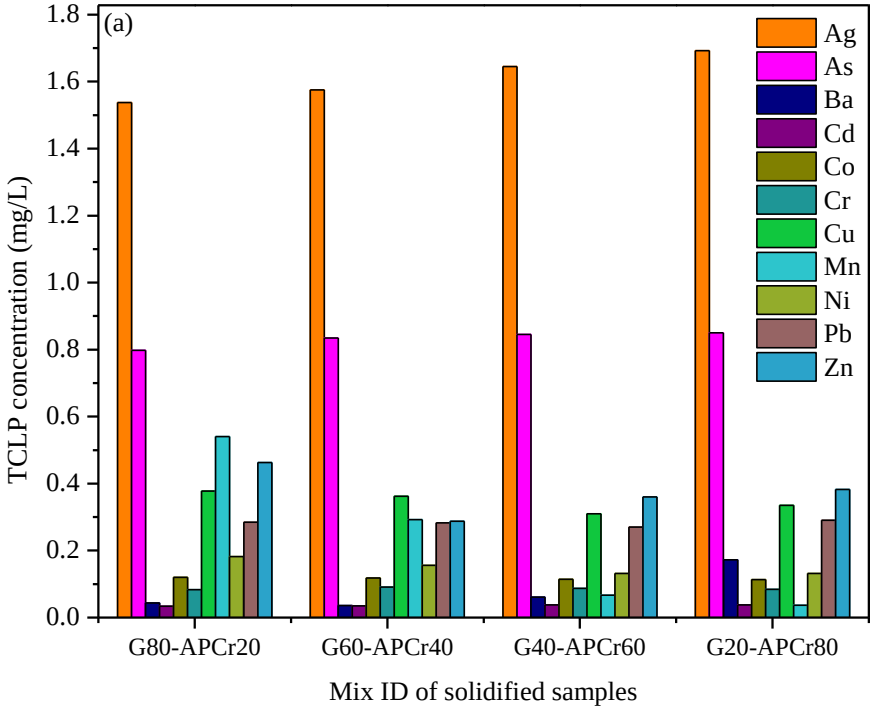

230

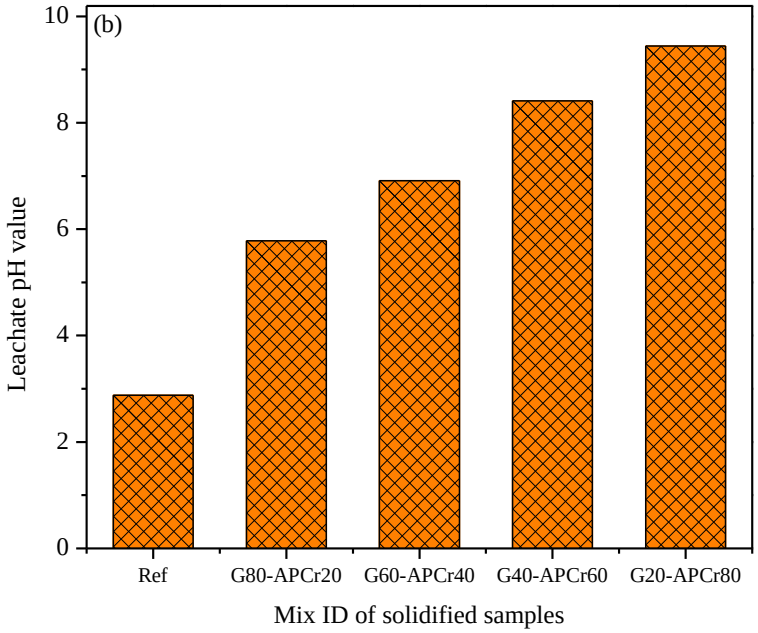

231

232 Fig. 1. TCLP results of Solidified samples (a) total concentration of heavy metals; (b) pH value
233 of leachate

234 The pH values of leachates of TCLP extracted samples are shown in Fig. 1b. Leachate pH value
235 is one of the key factors and provides important information about the immobilization efficiency
236 of cementitious materials. The pH value of Ref. solution (buffer acetic acid solution) was 2.88±0.5.

After TCLP extraction, pH value was gradually increased with the increase in percentage of APCr and was in the range of 5.78 to 9.44. Similar results have been reported in past studies and an increase in pH value is associated with the acid buffering capacity of the alkaline nature of APCr waste and geopolymer. According to past studies, the heavy metals (Mn, Cu, Cd, Zn, and Pb) which follow the cationic leaching behavior showed the reduced leaching concentration under the higher pH environment (Luo et al., 2019; Zhang et al., 2016) whereas concentration of Ba and As increased with the increase in alkalinity. Results of the present study are in agreement with the previous findings as with the increase in pH, Mn and Zn leaching was reduced and Ba and As leaching was slightly increased. However, there were marginal differences in the leaching concentration of all solidified samples and all values were well below the upper limits.

3.2 Physical and mechanical properties of APCr solidified samples

Bulk density and water absorption of control and solidified samples measured after 28 days of ambient curing are shown in Fig. 2a. There was a marginal increase in density when the amount of APCr was increased from 0% to 80%, however, the addition of APCr considerably increased the water absorption of solidified samples. The density and water absorption of controls samples without APCr (G100-APCr0) were 1876 kg/m^3 and 18.9%, which were increased to 1921 kg/m^3 (2.3% increase) and 27.58% (31% increase) for the G20-APCr80. The density of geopolymer pastes in a similar range has been observed in previous studies. (Hui-Teng et al., 2021; Song et al., 2019). The increase in density of APCR solidified samples can be linked to the smaller particle size of APCr as compared to FA and GGBS as it can fill into micropores and slightly increase the packing density of solidified mixtures. The increase in water absorption of APCr samples is mainly due to the filler nature of APCr as it does not react in a geopolymer system. When the amount of relatively inert APCr is increased, reactive aluminosilicate precursors are reduced in similar

proportions and a relatively weaker geopolymer network structure with the lower strength (see Fig 2(b)) is formed, leading to the higher water absorption of samples.

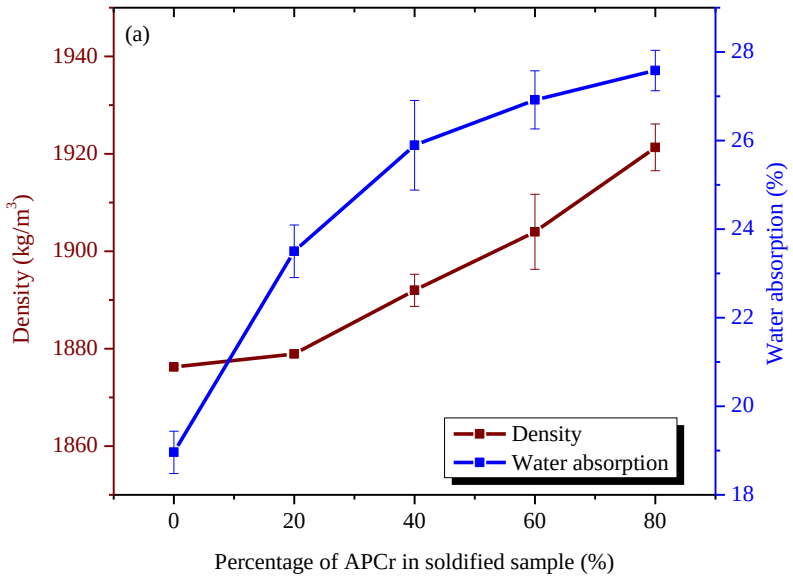

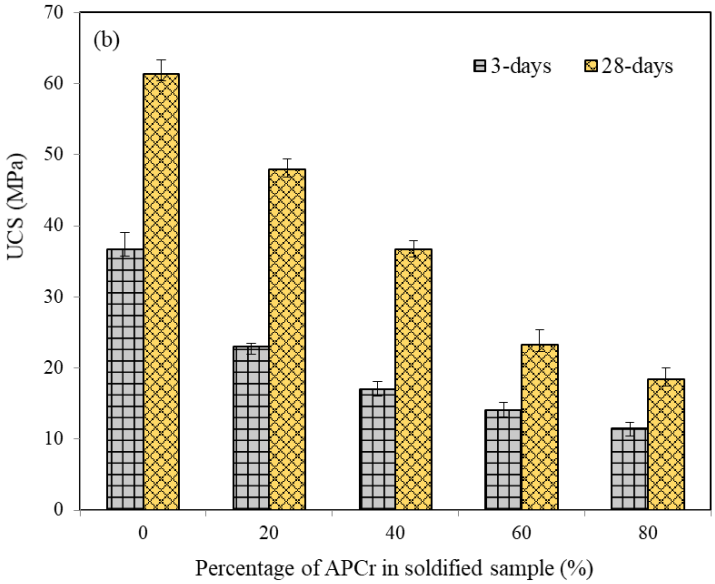

Fig. 2. Physical and mechanical properties of APCr solidified samples (a) Density and Water absorption; (b) Unconfined compressive strength (UCS)The results of unconfined compressive strength (UCS) for the APCr solidified samples are plotted in Fig. 2b. The pure geopolymer matrix (G100-APCr0) without APCr had the highest strength among all mixtures both at the age of 3 days

and 28 days. The UCS of G100-APCr0 was 36.7 MPa and 61.3 MPa at 3 days and 28 days, respectively. During the process of geopolymer reaction, there are several types of ions $[SiO_3(OH)]^{3-}$, $[SiO_2(OH)]^{-2}$, $[SiO(OH)]^{-}$ and $[AlO(OH)4]^{-}$) available to dissolve in an alkaline environment, which undergo polycondensation with Na and Ca cations to produce the three-dimensional network structure of geopolymer gels (N-A-S-H or C-A-S-H). The geopolymer gels are normally more compact than OPC based C-S-H gel and hence, make the geopolymer a stronger candidate for the solidification of hazardous wastes (Rasaki et al., 2019; Tian et al., 2020).

For the solidified APCr waste through GT, the UCS was significantly reduced gradually from 61.3 MPa to 18.4 MPa. The UCS for APCr solidified samples containing 20%, 40%, 60%, and 80% APCr was 47.9 MPa, 36.7 MPa, 23.3 MPa, and 18.4 MPa respectively. The decrease in the strength of APCr solidified samples was linked to the very low reactivity or filler nature of APCr (Li et al., 2017). This was because FA was gradually replaced by APCr for the solidification purpose and it contained a much lower amount of aluminosilicate phases (3.6% SiO_2 and 6.2% Al_2O_3) as compared to FA which could facilitate to form geopolymer gels (N/Ca-A-S-H) and contribute to strength development. Hence, as FA is replaced by APCr, the amount of aluminosilicate is also reduced in the solidified mixture and a lower amount of sodium aluminosilicate hydrates (N-A-S-H) were formed (Ali Shah et al., 2021; Yousefi Oderji et al., 2019). Results of the present study are compared with similar past studies conducted on the solidification of hazardous lead slag (Long et al., 2021a) and MSWI-FA (Fan et al., 2021) through FA-slag based geopolymer and FA based geopolymer respectively in Table 4. The comparison shows that GGBS-FA based geopolymer is more efficient in solidification of APCr than that of hazardous lead slag and MSWI-FA given that APCr solidified samples showed a superior strength even at a higher dosage of APCr waste (80%) and lower alkali content (5%).Table 4. Comparison of strength of APCr solidified samples with literature

Type of waste	% of waste by total mass	Precursor ratio (GGBS:FA)	UCS (MPa)	Na_2O/Precursor (%)
Hazardous lead slag (Long et al., 2021a)	33	1:0	18	10
	33	1:0.43	18	10
	33	1:1	17	10
	33	1:2.33	14.5	10
	33	0:1	5	10
MSWI-FA (Fan et al., 2021)	50	0:1	16.1	10
	60		18.1	10
	70		22.4	10
	80		18.7	10

	90		14.3	10
This study (APCr)	20	1:3	47.9	5
	40	1:2	36.7	5
	60	1:1	23.3	5
	80	1:0	18.4	5

3.3 TG/DTA results of APCr solidified bodies

The thermal stability of raw-APCr and APCr solidified samples was analyzed by the thermogravimetric analysis (TG-DTG-DTA curves) and results are shown in Fig. 3. The total mass loss for the raw-APCr from 30°C to 1000°C was 21.6%, The similar amount of (21%) mass loss was reported by the recent TGA study on APCr (Bogush et al., 2019). The mass of raw-APCr was quite stable up to 600°C and a sharp decrease was observed beyond that. DTG curve of raw-APCr showed three distinct peaks around 606°C (P2), 760°C (P3), and 891°C (P4). This loss in mass is linked to the endothermic peaks as shown in Fig. 3c around those temperatures. The loss in mass in between 600-760°C in primarily due to the decomposition of calcite ($CaCO_3$). Raw APCr had a mass loss of 3.39% in this temperature range. A broad peak around 891°C is associated with evaporation of Na, K, and Ca-based soluble salts containing sulfates and chlorides (Amutha Rani et al., 2008; Bogush et al., 2019).

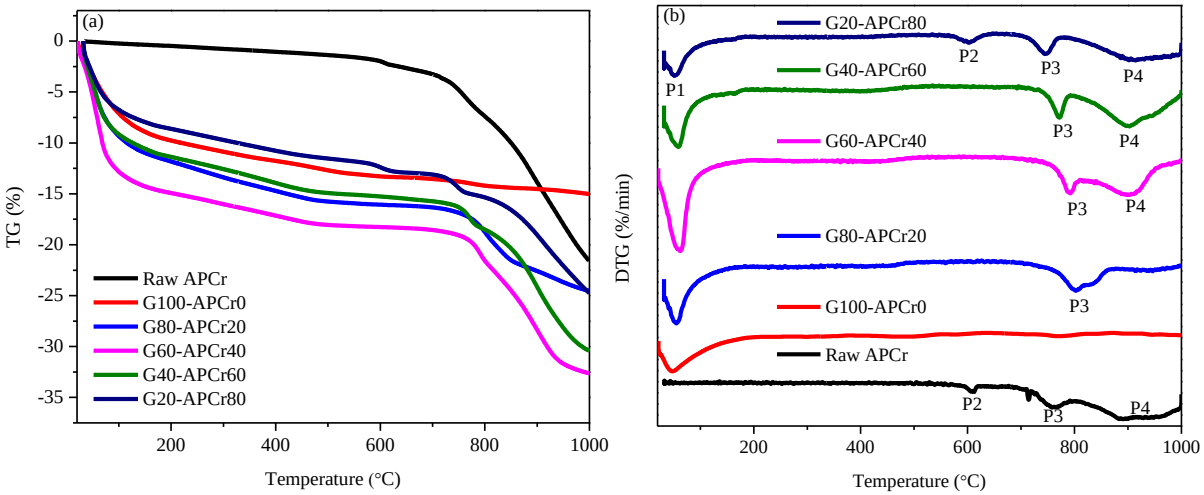

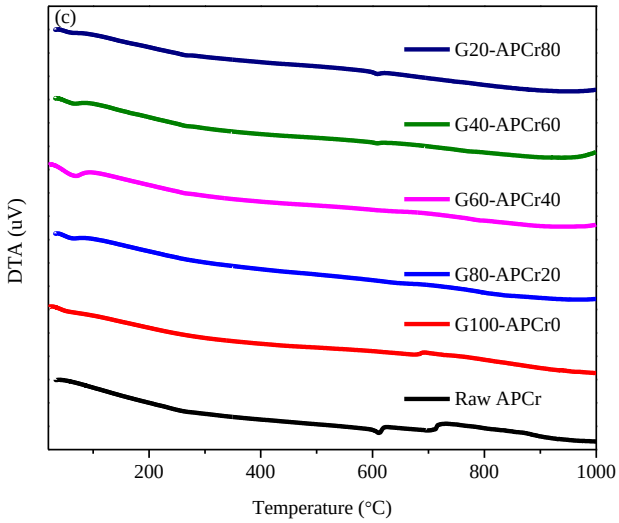

Fig. 3. Thermogravimetric analysis of APCr solidified samples (a) TG analysis; (b) DTG analysis; (c) DTA analysis. DTG and DTA curves are shifted for comparison purpose

For the control samples without APCr, there is only one distinct and broad peak (P1) as shown in DTG curve. The major loss in mass occurred from 30°C to 180°C. This loss in mass in control sample is attributed to evaporation of free water initially at lower temperatures and physically bound water (in C-S-H or N-(Ca)-S-H gels) at higher temperature up to 180°C (Hager et al., 2021; Kuri et al., 2021). The rate of mass loss was significantly reduced in the temperature range of 180°C to 1000°C. Mass loss for control sample was 9.5% from 30°C to 180°C and 5.5% from 180°C to 1000°C with the lowest total mass loss value of 15% among all samples. TG curves for the all APCr solidified samples showed the combination of raw-APCr and control sample and two prominent stages of loss in mass were seen in all solidified samples; (i) 30°C to 180°C and (ii) beyond 600°C. Mass loss was first increased with the increase in amount of APCr from 0% to 40% and then decreased with the further increase in amount of APCr from 40% to 80%. A sharp endothermic peak (P1) appeared in the G80-APCr20, becoming more deeper in G60-APCr40 and then again reduced in G40-APCr40 and G20-APCr80 (DTG curve Fig. 3b). Beyond 600°C, endothermic peaks (P2, P3, P4) started to reappear in the APCr solidified samples due to melting and evaporation of soluble salts present in the APCr. Between the 600-750°C, for the reference

mixture without APCr, mass loss was 0.58%. For the mixtures containing 20, 40, 60 and 80% APCr, mass lass was gradually increased to 0.99%, 1.02%, 1.43 and 2.42% respectively. Hence, this increase in mass loss is associated with the phase changes from APCr. It is important to mention that these peaks were shifted to the right side of their original position (although more distinct) due to geopolymerization process in solidified samples. The final loss in mass of solidified samples was higher than the control samples due to combined loss in mass of (i) free and physical bound water from geopolymer below 200ºC and (ii) evaporation of soluble salts from the APCr above 800ºC.

3.4 XRD analysis of APCr solidified samples

The phases in the solidified samples were characterized through the XRD analysis and results are shown in Fig. S5. The XRD pattern of control samples (G100-APCr0) without APCr showed only two types of distinct peaks namely quartz and calcite/C-S-H. The previous studies have also reported the presence of hump peak around 30° associated with C-(A)-S-H (Ababneh et al., 2019; Ahmad et al., 2021a), which could be formed due to the reaction of Ca (from CaO in GGBS) with the $[SiO_4]^{4-}$ either from raw materials or alkaline activator. Comparing the XRD patterns of precursor FA with control samples reveals that aluminosilicate present in raw FA were absent in the control sample, this indicates the dissolution of these aluminosilicate phases to form the geopolymer gel (N-A-S-H) in the presence of an alkaline activator. Partial dissolution of quartz and mullite in fly ash has been also reported in the literature as it further helps to improve the strength by formation of amorphous silica gel (Li et al., 2021). However, the geopolymer gel was hard to identify from the XRD pattern due to its amorphous nature and coexistence with the other crystalline phases (Xu et al., 2014). After FA was replaced with APCr into the geopolymer binder, new peaks appeared in the APCr solidified samples. Quartz peaks were gradually reduced and

eventually disappeared when amount of APCr was increased. For the 2θ value around 29°, calcite peak is present in the reference mixtures (0% APCr), and mixtures containing 20%, 40% and 80% APCr. Another calcite peak is identified in raw APCr around 55.6° 2θ. However, there is no calcite peak observed in the reference mixture (Figure S5) at the 2θ value of 55.6°. This calcite peak starts appearing as the percentage of APCr was gradually increased. This finding also corroborates the results of TGA analysis where an increase in loss mass was observed when the amount of APCr was increased (associated with the decomposition of calcite). New peaks in solidified samples originated from the APCr and became sharper with the increase in quantity of APCr. Peaks of thenardite (Na_2SO_4 peak around 18° and 34°), halite (NaCl peak around 32°) declined significantly as compared to peaks of raw APCr, which is linked to their partial dissolution into the water. Although, the use of Na_2SO_4 as a weak alkaline activator has been also reported in the literature (Alrefaei et al., 2020; Yang et al., 2021) however, Na_2SO_4 from APCr did not contribute to the improvement in strength in this study. This conclusion can be drawn from the linear decrease in strength of solidified samples with the increase in percentage of APCr.

3.5 FTIR analysis of APCr solidified samples

FTIR analysis results for the raw materials and APCr solidified samples are present in Fig. 4. Both FA and GGBS contain two bands associated with the tetrahedral AlO_4 and SiO_4 functional groups. A smaller wavelength band occurs around 450 cm^{-1} in FA and 480 cm^{-1} GGBS. The large wavelength bond occurs at 1054 cm^{-1} in FA and 900 cm^{-1} in GGBS. The shift of this band is linked to the higher degree of cross-linking of amorphous phase present in GGBS due to its high calcium amount (Pan et al., 2018). Two major bands in the APCr were observed at 1117 cm^{-1} and 615 cm^{-1} which were associated with asymmetrical stretching and asymmetrical bending vibration of SO_4 group respectively (Das et al., 2014).

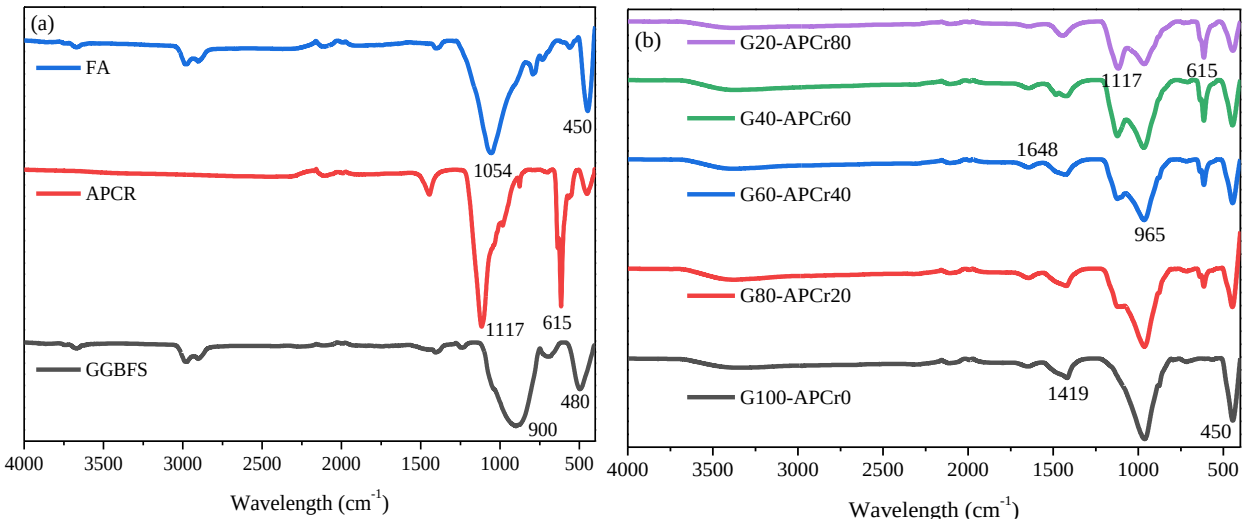

Fig. 4. FTIR analysis for (a) raw materials; (b) control sample and APCr solidified samples

For the control and APCr solidified samples, the presence of asymmetric stretching peak around 965 cm^{-1} was associated with the presence of geopolymer products (Ahmad et al., 2021b). This peak was due to presence of Si–O-T (T: tetrahedral Al or Si) and can be also viewed in the raw material (FA), however shifted to the lower wavelength for the geopolymer samples. This shift of T-O bands reveals that Al-Si or Si phases from the precursors had taken part in hydration reaction and produced geopolymer gel. The degree of geopolymerization in different samples can be accessed by the range of Si-O-T stretching peak (Nadeem et al., 2021) which is different for all samples as observed in Fig. 4b. Control samples had the highest degree of geopolymerization and the broader Si-O-T stretching peak. The range of stretching peak was gradually reduced with the increase of APCr amount, which confirms that the degree of geopolymerization was reduced. However, the presence of Si-O-T affirms the formation of geopolymer in all the samples, which played an important role in the solidification of APCr waste. Similar phenomenon was observed at the geopolymer band around 450 cm^{-1}. The absorption band at 1419 cm^{-1} corresponds to anti-symmetric stretching vibration of O-C-O bond of CO_3^{2-}. This band reflects the existence of carbonate as also spotted from the XRD analysis. A broad absorption band between the 3700 cm^{-}

^{1} and 3200 cm^{-1} is due to -OH stretching vibration whereas an absorption band around 1648 cm^{-1} is associated with the -OH bending vibration. For the samples containing APCr, peaks around 1117 cm^{-1} and 615 cm^{-1} started emerging and became more prominent when amount of APCr was increased from 20% to 80%.

3.6 SEM-EDS analysis of APCr and solidified samples

Distribution of different elements present in the APCr is captured by the SEM-EDS analysis and the elements spectrum and mapping are shown in Fig. S6. Two major elements (Na and S) were observed to be present in raw APCr powder and uniformly distributed. Other elements (Fe, Ca and Cl) were present in minor quantities. Mapping results of APCr are in line with the XRF, XRD, and FTIR results of raw-APCr as major elements and phases from these analysis techniques were also composed of Na and S.

Back-scattered electron images of control and APCr solidified samples analyzed through the SEM-EDS are provided in Fig. 5. The elemental compositions and spectrums for different points and areas are given in Table S1 and Fig. S7 (see supplementary data). For the control sample, presence of unreacted FA and reacted FA can be observed from Fig. 5a. Reaction of FA proves its dissolution in the alkaline environment which leads to the formation of geopolymer gel. While unreacted FA acts as a filler. Some of the unreacted GGBS particles are also observed. Formation of geopolymer gel was observed in area 1. The elemental composition showed that major elements present in area 1 are Ca, Na, Al, and Si. This indicates the co-existence of geopolymer gels (N-A-S-H and C-(A)-S-H). The co-existence of geopolymer gel (N-A-S-H) along with C-S-H gel has been reported in the metakaolin-GGBS based geopolymer previously (Yip et al., 2005). Sample containing 20% APCr (G80-APCr20) was analyzed for the given potential areas as marked in Fig. 5b. The presence of hematite, unreacted GGBS, mullite, and carbon was observed at the areas 2,

3, 5, and 6 respectively, while major elements at area 4 are Ca, Na, Al and Si which suggests the formation of geopolymer gel as also observed in control sample. Area 7 in G60-APCr40 samples (Fig. 5c) contains phases consisting of Ca-Al-Mg with ratio of 1:0.8:1.1. This phase seems to be weaker in strength and could be associated with elements from unreacted precursor. The formation of Fe-rich C-A-S-H and Fe-rich (N, C)-A-S-H gels are observed at area 8 and area 9 respectively. The elemental composition of FA is also obtained at area 10 to compare it with the geopolymer gels (Khedmati et al., 2018). The Si/Al and Na/Al ratios of FA are 1.25 and 0.03, respectively. In the geopolymer gel N-A-S-H, the Si/Al ratios at area 1, 4, 9 are 1.05, 1.22, and 0.64 while the Na/Al ratios are 0.29, 0.37 and 0.71, respectively. This shows that some of silica from the FA and GGBS precursors (area 3) has reacted with the alkaline activator. As percentage of APCr is further increased from 40% to 80% (Fig. 5d and Fig. 5e), presence of major elements (Na and S) from the APCr has increased in the solidified samples. The elemental composition at areas 11 and 13 indicates the combined presence of geopolymer gels and higher amounts of S, Na, P elements. This proves the interlocking effect of geopolymer gel to stabilize the APCr solidified waste even at a higher dosage. As APCr contained higher amount of Na element in its raw form, ratio of Na/Al was also increased from 0.29 to 1.39 gradually with the increase in percentage of APCr from 0% to 80% (area 1, 4, 9, 11, 13). The higher Si/Al ratio at area 11 and 13 is linked due to replacement of FA with the APCr as FA is major source of Al (while one source of silica (SS) was kept constant).

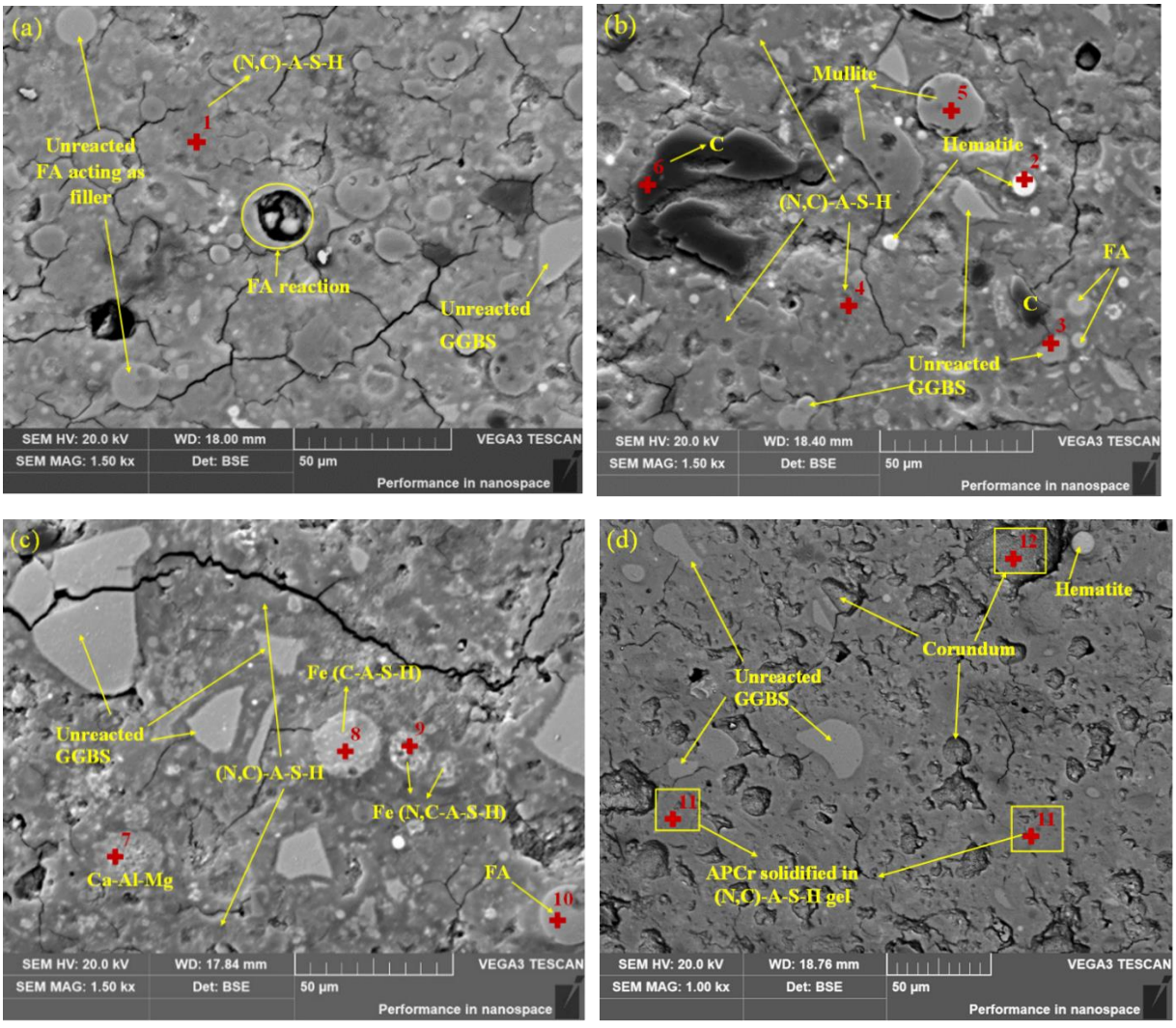
(a)
(N,C)-A-S-H
1
Unreacted
FA acting as
filler
FA reaction
Unreacted
GGBS
SEM HV: 20.0 kV
WD: 18.00 mm
VEGA3 TESCAN
SEM MAG: 1.50 kx
Det: BSE
50 µm
Performance in nanospace
(b)
Mullite
5
C
6
Hematite
2
(N,C)-A-S-H
4
FA
C
3
Unreacted
GGBS
SEM HV: 20.0 kV
WD: 18.40 mm
VEGA3 TESCAN
SEM MAG: 1.50 kx
Det: BSE
50 µm
Performance in nanospace
(c)
Fe (C-A-S-H)
Unreacted
GGBS
8
9
(N,C)-A-S-H
Fe (N,C-A-S-H)
7
Ca-Al-Mg
FA
10
SEM HV: 20.0 kV
WD: 17.84 mm
VEGA3 TESCAN
SEM MAG: 1.50 kx
Det: BSE
50 µm
Performance in nanospace
(d)
12
Hematite
Corundum
Unreacted
GGBS
11
11
APCr solidified in
(N,C)-A-S-H gel
SEM HV: 20.0 kV
WD: 18.76 mm
VEGA3 TESCAN
SEM MAG: 1.00 kx
Det: BSE
50 µm
Performance in nanospace

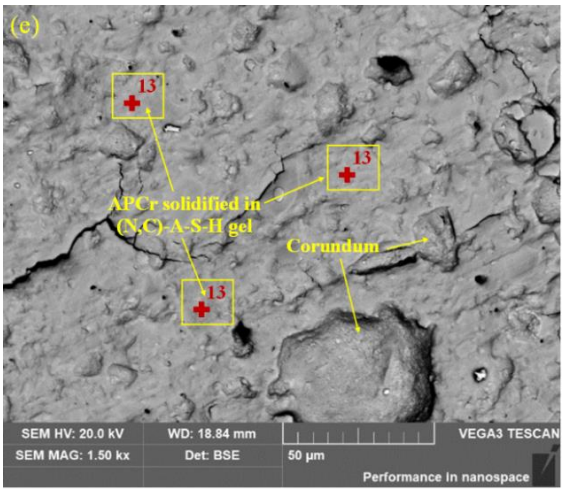

Fig. 5. SEM-EDS analysis of control and APCr solidified samples (a) G100-APCr0; (b) G20-APCr80; (c) G40-APCr60; (d) G60-APCr40 and (e) G80-APCr20 (Elemental compositions and EDS-spectrum of points/areas for Fig. 5 are shown in supplementary data information (Table S1 and Fig. S7)

3.7 EDS mapping of APCr solidified samples

Unreacted phases and homogeneity of geopolymer gel (distribution of Ca, Na, Al and Si element) were further investigated through the SEM-EDS mapping technique. The results for reference sample (G100-APCr0, 0% APCr) are shown in Fig. 6 while the mapping images of solidified samples containing 20%, 40%, 60% and 80% APCr are also shown in Fig. S8, S19, S10, and S11 respectively. The elemental composition and EDS spectrum of mapping for the control sample and all APCr solidified samples are given in Table S2 and Fig. S12. The major elements present in the G100-APCr0 are Ca (10.4%), Na (7.5%), Al (23.7%) and Si (48.9%) making almost 90% of the mapping area. These fours elements are uniformly distributed at similar locations and potentially form the geopolymer gel (N, Ca-Al-S-H). Some unreacted Ca was also observed in the mapping indicating the lower amount of formation of Ca-based hydration products (C-S-H/C-A-S-H) as compared to geopolymer gel (N-A-S-H). The Si/Al and Na/Al ratios in control sample are 2.07 and 0.32, respectively. Other unreacted phases consisted of Fe and Mg elements. Solidified samples containing 40% and 60% APCr closely followed the similar trend with the slightly

reduced Si/Al ratio of 1.32 and 1.67 as compared to control sample. This was due to replacement of APCr with FA which is major source of Si. However, the Na/Al ratio was increased to 0.39 and 0.67. The increase in Na/Al ratio was due to the higher content of alkaline content (Na_2O) in the APCr. This Na/Al ratio was further increased to 0.76 in G20-APCr80 sample. Solidified sample containing 80% APCr consists of Ca (12.2%), Na (18.3%), Al (24%) and Si (19.5%). These four elements make 74% of the mapping area. The presence of unreacted Ca was reduced whereas the amount of unreacted Al was increased in mapping area (Fig. S11.). This could indicate the lower degree of geopolymerization in the solidified samples containing a higher amount of APCr (80%) due to absence of aluminosilicate source (Fly ash). The higher content of Na appeared in the APCr, however, its contribution to improve the strength and formation of geopolymer product was negligible as compared to sodium metasilicate (i.e., the main alkaline activator). The elemental composition of G20-APCr80 sample suggests the presence of both C-(A)-S-H gel and N-A-S-H gel. The higher amount of S (11.8%) and P (5.7%) elements was observed and thoroughly distributed in the APCr solidified sample showing that geopolymer even at a lower content could still potentially act as a strong stabilizing agent.

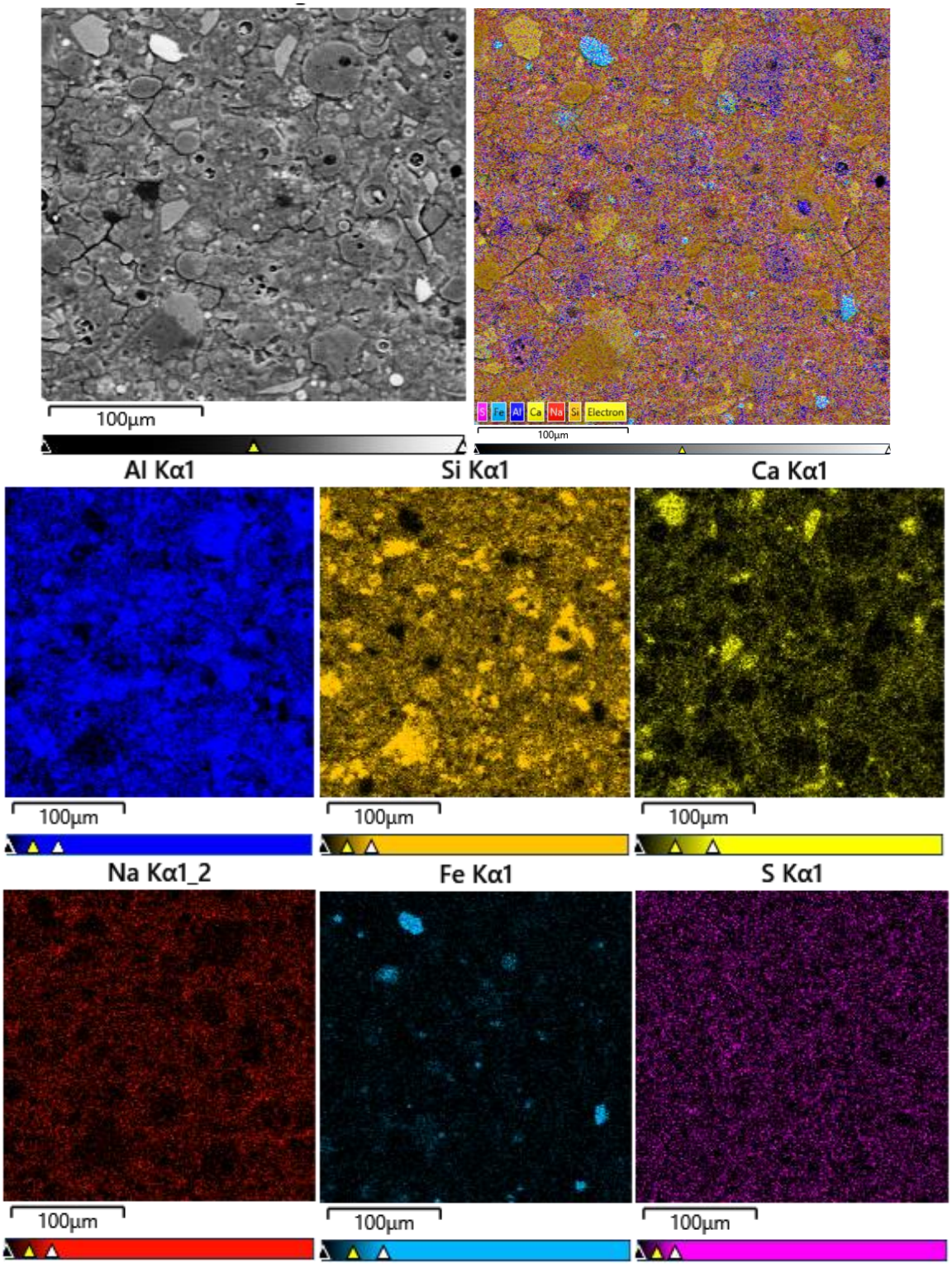

Fig. 6. SEM-EDS Mapping of control sample without APCr (G100-APCr0)

The solidified samples containing 80% APCr showed the crack of width of approximately 10 μm. A further investigation was conducted at the interface of crack through the EDS line scanning as shown in Fig. S13. It can be observed that the nature of hydration products are similar on both sides of the crack. Moreover, the formation of low strength geopolymer gel was suggested by EDS spectrum on the both side of crack. Hence, the appearance of such crack could be attributed to (a) crushing of sample during the compressive strength test, (b) force applied on the sample during the sample preparing or polishing process or (c) shrinkage of paste during drying process.

4 Conclusion

In this study, heavy metals in the APCr waste were stabilized/solidified using geopolymer technology. The percentage of APCr waste was increased from 20% to 80% by total weight of solids in the solidified samples. Characterization of solidified samples was performed using TCLP, UCS, XRD, TGA, FTIR, and SEM-EDS analyses. It was found that geopolymer based materials could help to solidify the larger amount of APCr (up to 80%) with high efficiency. Raw-APCr contained high concentrations of PTEs (e.g., Zn, Cu, Ba, Cr, and As). TCLP results showed the geopolymer was able to suppress the activity of these PTEs through S/S technique and the leaching values of all solidified samples fell well below the limits. An increase in the amount of APCr waste to replace FA had a negative influence on UCS. However, GT helped to retain 18.4 MPa even at the higher content of 80% of APCr by total weight in solidified samples, making them still applicable in engineering applications as low-medium strength construction materials. XRD results showed the dissolution of aluminosilicate phases of fly ash that formed the geopolymer gel, which helped to efficiently stabilize the PTEs. Thermal analysis results showed that APCr solidified samples started to lose mass significantly around 800°C due to melting and evaporation of soluble salts. The presence of geopolymer gel was observed in the control sample and all APCr

solidified samples by FTIR analysis. SEM-EDS analysis revealed the co-existence of N-A-S-H and C-(A)-S-H gels in the control samples. EDS analysis of solidified samples also indicated the formation of Fe-rich C-A-S-H and Fe-rich (N, C)-A-S-H gels at 20% and 40% of APCr content. A clear presence of unreacted S, P and Na elements was seen at the higher content of APCr, which were surrounded by the geopolymer products. Further research on the utilization of APCr as a replacement of filler materials or a weak alkaline activator (owing to its higher Na content) should be conducted in the future.

Author contribution statement

MR Ahmad: Conceptualization, Methodology, Investigation, Formal analysis, Writing - Original Draft. **JC Lao**: Methodology, Investigation, Writing. **JG DAI**: Conceptualization, Funding Acquisition, Supervision, Writing - Review & Editing. **DX Xuan:** Writing - Review & Editing **CS Poon**: Writing - Review & Editing

Acknowledgements

The authors would like to acknowledge the financial support received from NSFC/RGC Joint Research Scheme (N_PolyU542/20), The Hong Kong Polytechnic University through the Research Institute for Sustainable Urban Development (No.1-BBWE).

References

Ababneh, F.A., Alakhras, A.I., Heikal, M., Ibrahim, S.M., 2019. Stabilization of lead bearing sludge by utilization in fly ash-slag based geopolymer. Constr. Build. Mater. 227, 116694.

Ahmad, M.R., Chen, B., Ali Shah, S.F., 2021a. Mechanical and microstructural characterization of bio-concrete prepared with optimized alternative green binders. Constr. Build. Mater. 281, 122533. https://doi.org/https://doi.org/10.1016/j.conbuildmat.2021.122533

Ahmad, M.R., Chen, B., Haque, M.A., Oderji, S.Y., 2020a. Multiproperty characterization of cleaner and energy-efficient vegetal concrete based on one-part geopolymer binder. J. Clean. Prod. 253. https://doi.org/10.1016/j.jclepro.2019.119916

Ahmad, M.R., Chen, B., Haque, M.A., Saleem Kazmi, S.M., Munir, M.J., 2021b. Development of plant-concrete composites containing pretreated corn stalk bio-aggregates and different type of binders. Cem. Concr. Compos. 121, 104054. https://doi.org/https://doi.org/10.1016/j.cemconcomp.2021.104054

Ahmad, M.R., Chen, B., Haque, M.A., Shah, S.F.A., 2020b. Utilization of industrial and hazardous waste materials to formulate energy-efficient hygrothermal bio-composites. J. Clean. Prod. 250, 119469. https://doi.org/10.1016/j.jclepro.2019.119469

Ahmad, M.R., Chen, B., Shah, S.F.A., 2020c. Influence of different admixtures on the mechanical and durability properties of one-part alkali-activated mortars. Constr. Build. Mater. 265, 120320. https://doi.org/10.1016/j.conbuildmat.2020.120320

Alderete, N.M., Joseph, A.M., Van den Heede, P., Matthys, S., De Belie, N., 2021. Effective and sustainable use of municipal solid waste incineration bottom ash in concrete regarding strength and durability. Resour. Conserv. Recycl. 167, 105356. https://doi.org/https://doi.org/10.1016/j.resconrec.2020.105356

Ali Shah, S.F., Chen, B., Ahmad, M.R., Haque, M.A., 2021. Development of Cleaner One-part geopolymer from lithium slag. J. Clean. Prod. 291, 125241. https://doi.org/https://doi.org/10.1016/j.jclepro.2020.125241

Alrefaei, Y., Wang, Y.-S., Dai, J.-G., Xu, Q.-F., 2020. Effect of superplasticizers on properties of one-part Ca(OH)2/Na2SO4 activated geopolymer pastes. Constr. Build. Mater. 241, 117990. https://doi.org/https://doi.org/10.1016/j.conbuildmat.2019.117990

Amutha Rani, D., Gomez, E., Boccaccini, A.R., Hao, L., Deegan, D., Cheeseman, C.R., 2008. Plasma treatment of air pollution control residues. Waste Manag. 28, 1254–1262. https://doi.org/https://doi.org/10.1016/j.wasman.2007.06.008

Boca Santa, R.A.A., Soares, C., Riella, H.G., 2016. Geopolymers with a high percentage of bottom ash for solidification/immobilization of different toxic metals. J. Hazard. Mater. 318, 145–153. https://doi.org/https://doi.org/10.1016/j.jhazmat.2016.06.059

Bogush, A., Stegemann, J.A., Wood, I., Roy, A., 2015. Element composition and mineralogical characterisation of air pollution control residue from UK energy-from-waste facilities. Waste Manag. 36, 119–129. https://doi.org/https://doi.org/10.1016/j.wasman.2014.11.017

Bogush, A.A., Stegemann, J.A., Roy, A., 2019. Changes in composition and lead speciation due to water washing of air pollution control residue from municipal waste incineration. J. Hazard. Mater. 361, 187–199. https://doi.org/https://doi.org/10.1016/j.jhazmat.2018.08.051

Bogush, A.A., Stegemann, J.A., Zhou, Q., Wang, Z., Zhang, B., Zhang, T., Zhang, W., Wei, J., 2020. Co-processing of raw and washed air pollution control residues from energy-from-waste facilities in the cement kiln. J. Clean. Prod. 254, 119924. https://doi.org/https://doi.org/10.1016/j.jclepro.2019.119924

Chandler, A.J., Eighmy, T.T., Hjelmar, O., Kosson, D.S., Sawell, S.E., Vehlow, J., van der Sloot, H.A.,

Hartlén, J., 1997. Municipal solid waste incinerator residues. Elsevier.

Chang, J.-S., Cho, Y.-C., Lin, Y.-P., 2022. Regeneration of heavy metal contaminated soils for cement production by cement kiln co-processing. Resour. Conserv. Recycl. 176, 105909. https://doi.org/https://doi.org/10.1016/j.resconrec.2021.105909

Chen, L., Wang, Y.-S., Wang, L., Zhang, Y., Li, J., Tong, L., Hu, Q., Dai, J.-G., Tsang, D.C.W., 2021. Stabilisation/solidification of municipal solid waste incineration fly ash by phosphate-enhanced calcium aluminate cement. J. Hazard. Mater. 408, 124404.

Clavier, K.A., Ferraro, C.C., Townsend, T.G., 2021. Pilot-scale cement production using treated waste incineration bottom ash: physical and environmental performance. Resour. Conserv. Recycl. 175, 105862. https://doi.org/https://doi.org/10.1016/j.resconrec.2021.105862

CN-GB, 2007. Identification Standards for Hazardous Wastes-Identification for Extraction Toxicity (GB 5085.3-2007).

Cyr, M., Idir, R., Escadeillas, G., 2012. Use of metakaolin to stabilize sewage sludge ash and municipal solid waste incineration fly ash in cement-based materials. J. Hazard. Mater. 243, 193–203. https://doi.org/https://doi.org/10.1016/j.jhazmat.2012.10.019

Das, G., Kakati, N., Lee, S.H., Karak, N., Yoon, Y.S., 2014. Water soluble sodium sulfate nanorods as a versatile template for the designing of copper sulfide nanotubes. J. Nanosci. Nanotechnol. 14, 4455–4461.

EBHK, E.B. of H.K., 2013. BLUEPRINT FOR SUSTAINABLE USE OF RESOURCES [WWW Document]. URL https://www.enb.gov.hk/en/files/WastePlan-E.pdf (accessed 10.11.21).

EPA, U.S., 1992. Method 1311 Toxicity characteristic leaching procedure (TCLP). Agency EP, Ed. Washingt. DC, USA1992.

Fan, C., Wang, B., Ai, H., Qi, Y., Liu, Z., 2021. A comparative study on solidification/stabilization

591 characteristics of coal fly ash-based geopolymer and Portland cement on heavy metals in MSWI fly
592 ash. J. Clean. Prod. 319, 128790. https://doi.org/https://doi.org/10.1016/j.jclepro.2021.128790

593 Geng, C., Chen, C., Shi, X., Wu, S., Jia, Y., Du, B., Liu, J., 2020. Recovery of metals from municipal
594 solid waste incineration fly ash and red mud via a co-reduction process. Resour. Conserv. Recycl.
595 154, 104600. https://doi.org/https://doi.org/10.1016/j.resconrec.2019.104600

596 Gomes, H.I., Mayes, W.M., Rogerson, M., Stewart, D.I., Burke, I.T., 2016. Alkaline residues and the
597 environment: a review of impacts, management practices and opportunities. J. Clean. Prod. 112,
598 3571–3582. https://doi.org/https://doi.org/10.1016/j.jclepro.2015.09.111

599 Hager, I., Sitarz, M., Mróz, K., 2021. Fly-ash based geopolymer mortar for high-temperature application
600 – Effect of slag addition. J. Clean. Prod. 316, 128168.
601 https://doi.org/https://doi.org/10.1016/j.jclepro.2021.128168

602 Hui-Teng, N., Cheng-Yong, H., Yun-Ming, L., Abdullah, M.M.A.B., Ern Hun, K., Razi, H.M., Yong-
603 Sing, N., 2021. Formulation, mechanical properties and phase analysis of fly ash geopolymer with
604 ladle furnace slag replacement. J. Mater. Res. Technol. 12, 1212–1226.
605 https://doi.org/https://doi.org/10.1016/j.jmrt.2021.03.065

606 I., K., D., A.R., R., B.A., R., C.C., 2011. Geopolymers from DC Plasma–Treated Air Pollution Control
607 Residues, Metakaolin, and Granulated Blast Furnace Slag. J. Mater. Civ. Eng. 23, 735–740.
608 https://doi.org/10.1061/(ASCE)MT.1943-5533.0000170

609 Khedmati, M., Alanazi, H., Kim, Y.-R., Nsengiyumva, G., Moussavi, S., 2018. Effects of Na2O/SiO2
610 molar ratio on properties of aggregate-paste interphase in fly ash-based geopolymer mixtures
611 through multiscale measurements. Constr. Build. Mater. 191, 564–574.
612 https://doi.org/https://doi.org/10.1016/j.conbuildmat.2018.10.024

613 Kim, B., Lee, J., Kang, J., Um, W., 2021. Development of geopolymer waste form for immobilization of

radioactive borate waste. J. Hazard. Mater. 419, 126402. https://doi.org/https://doi.org/10.1016/j.jhazmat.2021.126402

Kourti, I., Rani, D.A., Deegan, D., Boccaccini, A.R., Cheeseman, C.R., 2010. Production of geopolymers using glass produced from DC plasma treatment of air pollution control (APC) residues. J. Hazard. Mater. 176, 704–709. https://doi.org/https://doi.org/10.1016/j.jhazmat.2009.11.089

Kozai, N., Sato, J., Osugi, T., Shimoyama, I., Sekine, Y., Sakamoto, F., Ohnuki, T., 2021. Sewage sludge ash contaminated with radiocesium: Solidification with alkaline-reacted metakaolinite (geopolymer) and Portland cement. J. Hazard. Mater. 416, 125965. https://doi.org/https://doi.org/10.1016/j.jhazmat.2021.125965

Kumar, V., Garg, N., 2022. The chemical and physical origin of incineration ash reactivity in cementitious systems. Resour. Conserv. Recycl. 177, 106009. https://doi.org/https://doi.org/10.1016/j.resconrec.2021.106009

Kuri, J.C., Majhi, S., Sarker, P.K., Mukherjee, A., 2021. Microstructural and non-destructive investigation of the effect of high temperature exposure on ground ferronickel slag blended fly ash geopolymer mortars. J. Build. Eng. 43, 103099. https://doi.org/https://doi.org/10.1016/j.jobe.2021.103099

Lange, L.C., Hills, C.D., Poole, A.B., 1995. Preliminary investigation into the effects of carbonation on cement-solidified hazardous wastes. Environ. Sci. Technol. 30, 25–30.

Leckner, B., 2015. Process aspects in combustion and gasification Waste-to-Energy (WtE) units. Waste Manag. 37, 13–25. https://doi.org/10.1016/J.WASMAN.2014.04.019

Li, J. shan, Xue, Q., Fang, L., Poon, C.S., 2017. Characteristics and metal leachability of incinerated sewage sludge ash and air pollution control residues from Hong Kong evaluated by different methods. Waste Manag. 64, 161–170. https://doi.org/10.1016/J.WASMAN.2017.03.033

637 Li, Y., Li, J., Cui, J., Shan, Y., Niu, Y., 2021. Experimental study on calcium carbide residue as a
638 combined activator for coal gangue geopolymer and feasibility for soil stabilization. Constr. Build.
639 Mater. 312, 125465. https://doi.org/https://doi.org/10.1016/j.conbuildmat.2021.125465

640 Liu, J., Hu, L., Tang, L., Ren, J., 2021. Utilisation of municipal solid waste incinerator (MSWI) fly ash
641 with metakaolin for preparation of alkali-activated cementitious material. J. Hazard. Mater. 402,
642 123451. https://doi.org/https://doi.org/10.1016/j.jhazmat.2020.123451

643 Loginova, E., Schollbach, K., Proskurnin, M., Brouwers, H.J.H., 2021. Municipal solid waste incineration
644 bottom ash fines: Transformation into a minor additional constituent for cements. Resour. Conserv.
645 Recycl. 166, 105354. https://doi.org/https://doi.org/10.1016/j.resconrec.2020.105354

646 Long, W.-J., Lin, C., Ye, T.-H., Dong, B., Xing, F., 2021a. Stabilization/solidification of hazardous lead
647 glass by geopolymers. Constr. Build. Mater. 294, 123574.
648 https://doi.org/https://doi.org/10.1016/j.conbuildmat.2021.123574

649 Long, W.-J., Peng, J., Gu, Y., Li, J., Dong, B., Xing, F., Fang, Y., 2021b. Recycled use of municipal solid
650 waste incinerator fly ash and ferronickel slag for eco-friendly mortar through geopolymer
651 technology. J. Clean. Prod. 307, 127281.
652 https://doi.org/https://doi.org/10.1016/j.jclepro.2021.127281

653 Luna Galiano, Y., Fernández Pereira, C., Vale, J., 2011. Stabilization/solidification of a municipal solid
654 waste incineration residue using fly ash-based geopolymers. J. Hazard. Mater. 185, 373–381.
655 https://doi.org/https://doi.org/10.1016/j.jhazmat.2010.08.127

656 Luo, H., Cheng, Y., He, D., Yang, E.-H., 2019. Review of leaching behavior of municipal solid waste
657 incineration (MSWI) ash. Sci. Total Environ. 668, 90–103.
658 https://doi.org/https://doi.org/10.1016/j.scitotenv.2019.03.004

659 Ma, W., Meng, F., Qiu, D., Tang, Y., 2020. Co-stabilization of Pb/Cu/Zn by beneficial utilization of

sewage sludge incineration ash: Effects of heavy metal type and content. Resour. Conserv. Recycl. 156, 104671. https://doi.org/https://doi.org/10.1016/j.resconrec.2019.104671

Mustard, G., Zhang, H., Ball, R.J., 2016. Stabilization of air pollution control residues by utilizing geopolymerisation to produce secondary building materials, in: 36th Cement and Concrete Science Conference.

Nadeem, M., Ahmed, F., Haq, E. ul, Zain-ul-Abdein, M., Raza, A., Afzal, U., Bibi, S., Deen, Z.S., 2021. Improved compressive strength and fracture toughness analysis of natural soil based geopolymer. J. Build. Eng. 44, 103241. https://doi.org/https://doi.org/10.1016/j.jobe.2021.103241

Nath, S.K., Randhawa, N.S., Kumar, S., 2022. A review on characteristics of silico-manganese slag and its utilization into construction materials. Resour. Conserv. Recycl. 176, 105946. https://doi.org/https://doi.org/10.1016/j.resconrec.2021.105946

Nguyen, T.A.H., Guo, X., You, F., Saha, N., Wu, S., Scheuermann, A., Ren, C., Huang, L., 2022. Co-solidification of bauxite residue and coal ash into indurated monolith via ambient geopolymerisation for in situ environmental application. J. Hazard. Mater. 422, 126925. https://doi.org/https://doi.org/10.1016/j.jhazmat.2021.126925

Pan, D., Li, L., Tian, X., Wu, Y., Cheng, N., Yu, H., 2019. A review on lead slag generation, characteristics, and utilization. Resour. Conserv. Recycl. 146, 140–155. https://doi.org/https://doi.org/10.1016/j.resconrec.2019.03.036

Pan, Z., Tao, Z., Cao, Y.F., Wuhrer, R., Murphy, T., 2018. Compressive strength and microstructure of alkali-activated fly ash/slag binders at high temperature. Cem. Concr. Compos. 86, 9–18.

Pu, S., Zhu, Z., Song, W., Wang, H., Huo, W., Zhang, J., 2021. A novel acidic phosphoric-based geopolymer binder for lead solidification/stabilization. J. Hazard. Mater. 415, 125659. https://doi.org/https://doi.org/10.1016/j.jhazmat.2021.125659

683 Qian, L.-P., Xu, L.-Y., Alrefaei, Y., Wang, T., Ishida, T., Dai, J.-G., 2022. Artificial alkali-activated
684 aggregates developed from wastes and by-products: A state-of-the-art review. Resour. Conserv.
685 Recycl. 177, 105971. https://doi.org/https://doi.org/10.1016/j.resconrec.2021.105971

686 Quina, M.J., Bordado, J.M., Quinta-Ferreira, R.M., 2014. Recycling of air pollution control residues from
687 municipal solid waste incineration into lightweight aggregates. Waste Manag. 34, 430–438.
688 https://doi.org/https://doi.org/10.1016/j.wasman.2013.10.029

689 Rasaki, S.A., Bingxue, Z., Guarecuco, R., Thomas, T., Minghui, Y., 2019. Geopolymer for use in heavy
690 metals adsorption, and advanced oxidative processes: A critical review. J. Clean. Prod. 213, 42–58.
691 https://doi.org/https://doi.org/10.1016/j.jclepro.2018.12.145

692 Shirley, R., Black, L., 2011. Alkali activated solidification/stabilisation of air pollution control residues
693 and co-fired pulverised fuel ash. J. Hazard. Mater. 194, 232–242.
694 https://doi.org/https://doi.org/10.1016/j.jhazmat.2011.07.100

695 Song, W., Zhu, Z., Peng, Y., Wan, Y., Xu, X., Pu, S., Song, S., Wei, Y., 2019. Effect of steel slag on
696 fresh, hardened and microstructural properties of high-calcium fly ash based geopolymers at
697 standard curing condition. Constr. Build. Mater. 229, 116933.
698 https://doi.org/https://doi.org/10.1016/j.conbuildmat.2019.116933

699 Stegemann, J.A., 2014. The potential role of energy-from-waste air pollution control residues in the
700 industrial ecology of cement. J. Sustain. Cem. Mater. 3, 111–127.

701 Sun, J., Wang, L., Yu, J., Guo, B., Chen, L., Zhang, Y., Wang, D., Shen, Z., Tsang, D.C.W., 2022.
702 Cytotoxicity of stabilized/solidified municipal solid waste incineration fly ash. J. Hazard. Mater.
703 424, 127369. https://doi.org/https://doi.org/10.1016/j.jhazmat.2021.127369

704 Sun, Y., Hu, S., Zhang, P., Elmaadawy, K., Ke, Y., Li, J., Li, M., Hu, J., Liu, B., Yang, J., Liang, S.,
705 Xiao, K., Hou, H., 2020. Microwave enhanced solidification/stabilization of lead slag with fly ash

based geopolymer. J. Clean. Prod. 272, 122957. https://doi.org/https://doi.org/10.1016/j.jclepro.2020.122957

Tang, P., Chen, W., Xuan, D., Cheng, H., Poon, C.S., Tsang, D.C.W., 2020. Immobilization of hazardous municipal solid waste incineration fly ash by novel alternative binders derived from cementitious waste. J. Hazard. Mater. 393, 122386.

Tian, X., Rao, F., Morales-Estrella, R., Song, S., 2020. Effects of Aluminum Dosage on Gel Formation and Heavy Metal Immobilization in Alkali-Activated Municipal Solid Waste Incineration Fly Ash. Energy & Fuels 34, 4727–4733. https://doi.org/10.1021/acs.energyfuels.9b04493

US EPA, 2004. Characteristics Introduction and Regulatory Definitions, Test Methods for Evaluating Solid Waste, Physical/Chemical Methods (SW 846), US Environmental Protection Agency. [WWW Document].

Van De Sande, J., Peys, A., Hertel, T., Rahier, H., Pontikes, Y., 2020. Upcycling of non-ferrous metallurgy slags: Identifying the most reactive slag for inorganic polymer construction materials. Resour. Conserv. Recycl. 154, 104627. https://doi.org/https://doi.org/10.1016/j.resconrec.2019.104627

Wang, F.-H., Zhang, F., Chen, Y.-J., Gao, J., Zhao, B., 2015. A comparative study on the heavy metal solidification/stabilization performance of four chemical solidifying agents in municipal solid waste incineration fly ash. J. Hazard. Mater. 300, 451–458. https://doi.org/https://doi.org/10.1016/j.jhazmat.2015.07.037

Wang, Lei, Chen, L., Guo, B., Tsang, D.C.W., Huang, L., Ok, Y.S., Mechtcherine, V., 2020. Red mud-enhanced magnesium phosphate cement for remediation of Pb and As contaminated soil. J. Hazard. Mater. 400, 123317.

Wang, Liuwei, Li, X., Tsang, D.C.W., Jin, F., Hou, D., 2020. Green remediation of Cd and Hg

contaminated soil using humic acid modified montmorillonite: Immobilization performance under accelerated ageing conditions. J. Hazard. Mater. 387, 122005.

Wang, Y.-S., Alrefaei, Y., Dai, J.-G., 2020. Influence of coal fly ash on the early performance enhancement and formation mechanisms of silico-aluminophosphate geopolymer. Cem. Concr. Res. 127, 105932.

Wang, Y.-S., Alrefaei, Y., Dai, J.-G., 2019. Silico-aluminophosphate and alkali-aluminosilicate geopolymers: A comparative review. Front. Mater. 6, 106.

Woon, K.S., Lo, I.M.C., 2013. Greenhouse gas accounting of the proposed landfill extension and advanced incineration facility for municipal solid waste management in Hong Kong. Sci. Total Environ. 458–460, 499–507. https://doi.org/https://doi.org/10.1016/j.scitotenv.2013.04.061

Xi, B., Yang, T., Zhao, R., Jing, L., Gong, T., Huang, Q., Hou, L., 2021. Hazardous Waste Management in the Guangdong–Hong Kong–Macao Greater Bay Area. Engineering. https://doi.org/https://doi.org/10.1016/j.eng.2021.08.009

Xu, B., Winnefeld, F., Lothenbach, B., 2021. Effect of temperature curing on properties and hydration of wollastonite blended magnesium potassium phosphate cements. Cem. Concr. Res. 142, 106370. https://doi.org/https://doi.org/10.1016/j.cemconres.2021.106370

Xu, H., Gong, W., Syltebo, L., Izzo, K., Lutze, W., Pegg, I.L., 2014. Effect of blast furnace slag grades on fly ash based geopolymer waste forms. Fuel 133, 332–340.

Xuan, D., Poon, C.S., 2018. Removal of metallic Al and Al/Zn alloys in MSWI bottom ash by alkaline treatment. J. Hazard. Mater. 344, 73–80.

Yang, G., Wu, T., Fu, C., Ye, H., 2021. Effects of activator dosage and silica fume on the properties of Na2SO4-activated high-volume fly ash. Constr. Build. Mater. 278, 122346. https://doi.org/https://doi.org/10.1016/j.conbuildmat.2021.122346

752 Yip, C.K., Lukey, G.C., van Deventer, J.S.J., 2005. The coexistence of geopolymeric gel and calcium
753 silicate hydrate at the early stage of alkaline activation. Cem. Concr. Res. 35, 1688–1697.
754 https://doi.org/https://doi.org/10.1016/j.cemconres.2004.10.042

755 Yousefi Oderji, S., Chen, B., Ahmad, M.R., Shah, S.F.A., 2019. Fresh and hardened properties of one-
756 part fly ash-based geopolymer binders cured at room temperature: Effect of slag and alkali
757 activators. J. Clean. Prod. 225, 1–10. https://doi.org/10.1016/j.jclepro.2019.03.290

758 Zentar, R., Wang, H., Wang, D., 2021. Comparative study of stabilization/solidification of dredged
759 sediments with ordinary Portland cement and calcium sulfo-aluminate cement in the framework of
760 valorization in road construction material. Constr. Build. Mater. 279, 122447.
761 https://doi.org/https://doi.org/10.1016/j.conbuildmat.2021.122447

762 Zhang, H., Zhao, Y., Hou, D., Hao, H., 2022. Cementitious binders modified with halloysite nanotubes
763 for enhanced lead immobilization. Powder Technol. 395, 149–157.
764 https://doi.org/https://doi.org/10.1016/j.powtec.2021.09.068

765 Zhang, P., Muhammad, F., Yu, L., Xia, M., Lin, H., Huang, X., Jiao, B., Shiau, Y., Li, D., 2020. Self-
766 cementation solidification of heavy metals in lead-zinc smelting slag through alkali-activated
767 materials. Constr. Build. Mater. 249, 118756.
768 https://doi.org/https://doi.org/10.1016/j.conbuildmat.2020.118756

769 Zhang, Y., Cetin, B., Likos, W.J., Edil, T.B., 2016. Impacts of pH on leaching potential of elements from
770 MSW incineration fly ash. Fuel 184, 815–825.
771 https://doi.org/https://doi.org/10.1016/j.fuel.2016.07.089

772 Zhuang, H., Guan, J., Leu, S.-Y., Wang, Y., Wang, H., 2020. Carbon footprint analysis of chemical
773 enhanced primary treatment and sludge incineration for sewage treatment in Hong Kong. J. Clean.
774 Prod. 272, 122630. https://doi.org/https://doi.org/10.1016/j.jclepro.2020.122630

775

776

777

778

779

780

781

782

783

784

785